https://doi.org/10.5194/egusphere-2025-603
Preprint. Discussion started: 28 March 2025

Ephemeral grounding on the Pine Island Ice Shelf, West Antarctica, from 2014 to 2023

Yide Qian[1,2,3], Chunxia Zhou[1,2,3*], Sainan Sun[4], Yiming Chen[1,2], Tao Wang[1,2], Baojun Zhang[1,2,3]

[1]Chinese Antarctic Center of Surveying and Mapping, Wuhan University, Wuhan, 430079, China
[2]Key Laboratory of Polar Environment Monitoring and Public Governance (Wuhan University), Ministry of Education, Wuhan, 430079 China
[3]School of Geodesy and Geomatics, Wuhan University, Wuhan, 430079 China
[4]Department of Geography and Environmental Sciences, Northumbria University, Newcastle upon Tyne, NE1 8ST, UK

Correspondence to: Chunxia Zhou (zhoucx@whu.edu.cn)

Abstract. Ephemeral grounding sites form when ice shelves thin or relative sea level rises, causing pinning points to ground intermittently over tidal cycles. Vertical displacements derived from Sentinel-1A/B imagery reveal the ephemeral grounding history of the Pine Island Ice Shelf from 2014 to 2023. We found that the ephemeral grounding site disappeared after the ice shelf calved in 2020 and appeared again after October 2021. We conclude that basal melting directly influences the occurrence of ephemeral grounding at the central ice shelf. Ice shelf calving and atmospheric forcings, such as La Niña and the positive phase of the Antarctic Oscillation, are indirect factors that affect ephemeral grounding. We propose that the ephemeral grounding site at the central ice shelf may evolve into a final pinning point and may influence future ice shelf calving events. Further studies on ice shelf modeling are needed to understand the interaction between ephemeral grounding and rift propagation.

1 Introduction

Ice discharge from the Antarctic Ice Sheet is a major contributor to global sea-level rise. (Shepherd et al., 2012; Bamber et al., 2018; Smith et al., 2020). Ice shelves act as crucial buttresses, resisting the flow of inland ice into the ocean. However, ice shelf thinning and retreat have significantly reduced their buttressing capacity, leading to accelerated ice discharge and an increased contribution to sea-level rise (Rott et al., 2002, 2018; Rignot et al., 2004; Pritchard et al., 2012; Fürst et al., 2016; Gudmundsson et al., 2019; Joughin et al., 2021). This buttressing effect is primarily controlled by resistive forces, including lateral drag along embayment walls and the resistance offered by pinning points, where ice shelves ground on elevated seafloor features (Matsuoka et al., 2015; Alley et al., 2015).

Pinning points are critical in modulating ice shelf dynamics (Matsuoka et al., 2015). Their evolution, particularly changes in size and location, can significantly influence ice flow by inducing lateral and basal shear stresses, as well as upstream compression and downstream tension (Fried et al., 2014; Still et al., 2019, 2021). Additionally, pinning points can promote rifting and calving, further reducing buttressing (Arndt et al., 2018), and can alter sub-ice shelf ocean circulation and basal

https://doi.org/10.5194/egusphere-2025-603
Preprint. Discussion started: 28 March 2025

melt patterns (Milillo et al., 2019; Shean et al., 2019). Over time, some pinning points have disappeared entirely, particularly since 1973 (Milles and Bingham, 2024). As ice shelves thin or relative sea levels rise, these features may transition into ephemeral grounding sites, where grounding occurs only intermittently during tidal cycles (Schmeltz et al., 2001; Rignot, 2002; Matsuoka et al., 2015). Although the direct buttressing effect of ephemeral grounding sites is minimal, their presence and evolution provide valuable insights into changes in ice shelf thickness and basal drag, which can influence surface elevation and larger-scale ice shelf dynamics (Rignot, 2002; Christianson et al., 2016; Jeong et al., 2016; Shean, 2016).

A prominent example of ephemeral grounding is ice rumple L, a 0.5-km-diameter feature on the central Pine Island Ice Shelf (PIIS) (Figure 1). First observed in 2011 using differential interferometry (Rignot et al., 2014), ice rumple L is believed to have become ephemerally grounded in the 1940s and fully ungrounded between 1973 and 1989 (Jenkins et al., 2010; Smith et al., 2017; Milles and Bingham, 2024). This ungrounding has been attributed to increased basal melting caused by the intrusion of warm Circumpolar Deep Water (CDW) (Jenkins et al., 2010; Jacobs et al., 2011; Pritchard et al., 2012; Hillenbrand et al., 2017; Smith et al., 2017; Davies et al., 2017; Shean et al., 2019). Ice rumple L reappeared after 2011, and its recurring cycle of ephemeral grounding is now understood to result from interactions between sub-ice shelf keels and an underlying submarine ridge (Graham et al., 2013; Joughin et al., 2016; Shean, 2016; Davies et al., 2017). After four calving events occurred between 2015 and 2020 (Jeong et al., 2016; Arndt et al., 2018; Qi et al., 2021), specifically on 13 July 2015, 12 October 2017, 31 October 2018, and 11 February 2020, the changes to ice rumple L remain unclear.

Vertical motion of ice shelves, particularly tidal fluctuations associated with ephemeral grounding, can be observed using several satellite techniques, including differential range offset tracking (DROT) (Marsh et al., 2013; Joughin et al., 2016; Christianson et al., 2016; Wallis et al., 2024), interferometric synthetic aperture radar (InSAR) (Schmeltz et al., 2001; Rignot, 2002, 2014), and altimetry (Fricker and Padman, 2006). However, the rapid motion of ice shelves presents a challenge for traditional InSAR, requiring very short repeat cycles to avoid phase aliasing (Rignot et al., 2014; Scheuchl et al., 2016; Milillo et al., 2017). For instance, Milillo et al. (2017) used 1-day repeat COSMO-SkyMed data to study grounding line changes at PIIS. DROT offers an alternative, as it does not rely on phase information. This makes it particularly well-suited for observing vertical tidal displacements on fast-moving ice shelves, even though it may be less precise than InSAR (Marsh et al., 2013; Hogg, 2015; Joughin et al., 2016; Friedl et al., 2020; Wallis et al., 2024). Joughin et al. (2016), using DROT with TerraSAR-X SM data (11- or 22-day repeat, ~3 m range resolution), identified a vertical displacement anomaly near ice rumple L, achieving a grounding line position precision of approximately 1.5 km. More recently, Friedl et al. (2020) and Wallis et al. (2024) have demonstrated the effectiveness of DROT with Sentinel-1 IW data for grounding line studies. According to Friedl et al. (2020), DROT-derived grounding line positions (tidal flexure limit) were ~2 km seaward of DInSAR and ~2 km landward of H positions, where is the landward limit of stable hydrostatic equilibrium.

To address the knowledge gap regarding the relationship between changes of ice rumple L and ice shelf dynamics at PIIS, particularly in the period following four recent calving events and an observed increase in ice velocity from 2014 to 2023, we analyze double-differential vertical displacement derived from Sentinel-1 SAR data, which provides consistent spatial and temporal coverage of the region. Combined with time series of ice thickness change from 2010 to 2021 derived from

https://doi.org/10.5194/egusphere-2025-603
Preprint. Discussion started: 28 March 2025

REMA DEM (Howat et al., 2022a), we aim to reconstruct the ephemeral grounding history of the PIIS from 2014 to 2023 and investigate the influence of calving, oceanic forcing and atmospheric forcings on ephemeral grounding.

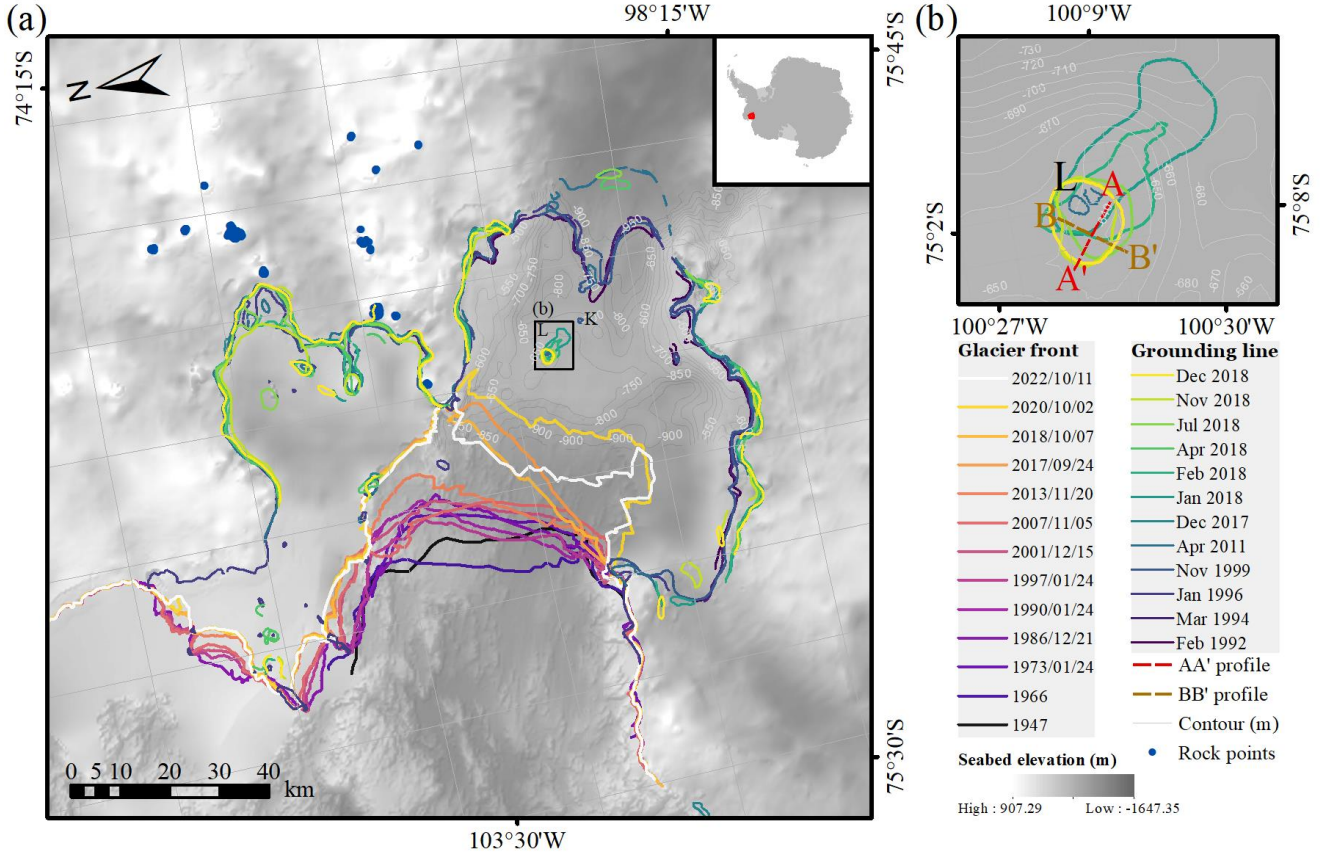

Figure 1. Location and geometry of the PIIS. (a) Ice front positions, grounding line locations, and 458 non-glaciated ground control points (blue) on the PIIS. (b) Ice rumple L, the 2011 grounding line, and profiles AA' and BB' used for ice-equivalent freeboard thickness change analysis. Bathymetry (50 m contour interval, labeled between -750 m and -500 m) is from BedMachine v3 (Morlighem et al., 2020; Morlighem, 2022), showing the submarine ridge. Grounding lines are from MEaSUREs (Rignot et al., 2016), ESA CCI (Floricioiu et al., 2021), and Mohajerani et al. (2021). L and K mark ice rumples (Rignot et al., 2014). Ice front positions for 1947 and 1966 are from Rignot (2002); later positions (1973-2022) are from Landsat panchromatic imagery and Sentinel-1 SAR imagery via Google Earth Engine.

2 Methods and Data

2.1 Double-differential vertical displacement calculation

Vertical displacement maps were generated for the Pine Island Glacier (PIG) basin using the intensity offset tracking algorithm in GAMMA software. This involved applying the algorithm to 426 scenes of Sentinel-1A/B ascending imagery, covering periods of 6- or 12-days from October 2014 to December 2023. Details of the imagery used are provided in Table 1. We applied fine coregistration and deramping procedures prior to offset tracking (Wegmüller et al., 2016; Sánchez-Gámez et al., 2017; Chen et al., 2020). We used the REMA dataset (Howat et al., 2019; 2022b), which is posted on a 200 m grid, as the

https://doi.org/10.5194/egusphere-2025-603
Preprint. Discussion started: 28 March 2025

reference DEM for geocoding and coregistering the Sentinel-1 imagery. To compute the displacement fields from the coregistered and deramped imagery, we propose a 2D cross-correlation window of 480×96 (range × azimuth) pixels with step sizes of 100 and 20 pixels in the azimuth and range directions, respectively. We used the REMA DEM to geocode the displacement maps based on bicubic-log spline interpolation. The final vertical displacement maps and velocity maps were generated on 100 m×100 m grids and geocoded to the Antarctic Polar Stereographic Projection (EPSG:3031).

Path/frame	Date	Numbers
65/909	2014/10/10 – 2015/11/10	30
	2016/05/20 – 2017/06/20	50
65/908	2015/11/22 – 2016/07/07	18
65/911	2017/06/14 – 2017/10/18	20
65/910	2017/10/24 – 2021/12/20	250
	2022/01/01 – 2024/01/03	58
	Total	426

Table 1. Sentinel-1A/B images used in this study

To reduce noise and remove outliers (Paul et al., 2015; Lemos et al., 2018; Solgaard et al., 2021; Lei et al., 2021), we first accepted pixels with an NCC greater than 0.05. Second, we extracted the residual displacement at 458 widely distributed, non-moving points over the exposed bedrock (Figure 1(a)), removed outliers beyond one standard deviation, and calculated the mean value for each time interval. Third, we calibrated the ice displacement by subtracting the mean value of the residual displacement. Finally, we examined the entire time series and identified the highest and lowest displacement values. We then invalidated pixels with the following criteria: azimuth displacement values less than -30 m or greater than 90 m for a 6-day gap; azimuth displacement values less than -60 m or greater than 180 m for a 12-day gap; range displacement values less than -60 m or greater than 75 m for a 6-day gap; and range displacement values less than -120 m or greater than 150 m for a 12-day gap.

The slant range displacement fields generated over floating ice contain both horizontal displacement and bias due to vertical ocean motion. When the SAR sensor observes an object $P_{(x,y)}$ from the same location in orbit, the SAR sensor can detect vertical displacement in the slant range direction ($\Delta D_{sr(t_2,t_1)}$ in Figure 2):

$$\Delta D_{sr(t_2,t_1)} = D_{sr(t_2)} - D_{sr(t_1)}\,, \tag{1}$$

where D_{sr} is the distance between the object $P_{(x,y)}$ and the SAR sensor; t_1 and t_2 reflect the acquisition time of the master image and the acquisition time of the slave image, respectively. The magnitude of the observed slant range displacement

https://doi.org/10.5194/egusphere-2025-603
Preprint. Discussion started: 28 March 2025

depends on the local incidence angle (θ_{inc}). When the slant range displacement is converted to ground range displacement, the additional displacement in the ground range ($\Delta D_{gr(t_2,t_1)}$) equals the vertical change ($\Delta h_{\perp(t_2,t_1)}$) divided by $\tan\theta_{inc}$:

$$\Delta D_{gr(t_2,t_1)} = \frac{\Delta h_{\perp(t_2,t_1)}}{\tan\theta_{inc}}, \quad (2)$$

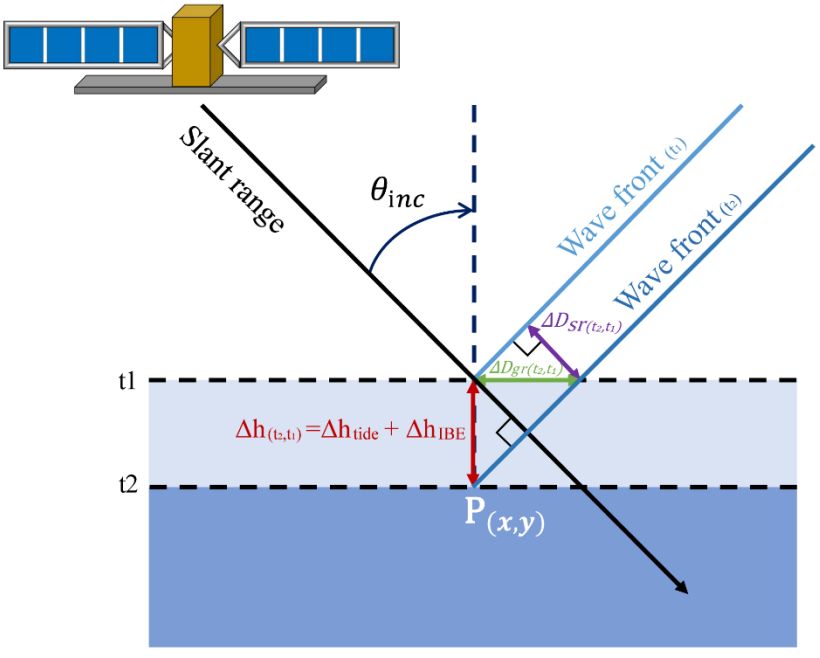

Figure 2. Side-looking spaceborne SAR imaging geometry. A vertical displacement of a Point $P_{(x,y)}$ from t_1 to t_2 is imaged at different slant range positions ($\mathbf{\Delta D_{sr(t_2,t_1)}}$) depending on its elevation.

Assuming that the horizontal displacement between two SAR image pairs that are closely spaced in time is very small, we can cancel the horizontal displacement and obtain the differential vertical bias in the ground range (ΔDD_{gr}) by differencing two ground range displacement fields (Rignot, 1998; Joughin et al., 2010; Marsh et al., 2013; Christianson et al., 2016; Joughin et al., 2016; Friedl et al., 2020):

$$\Delta DD_{gr} = \Delta D_{gr(t3,t2)} - \Delta D_{gr(t2,t1)}, \quad (3)$$

where $\Delta D_{gr(t_2,t_1)}$ and $\Delta D_{gr(t_3,t_2)}$ are the vertical displacement differences in the ground range direction from the displacement map generated from the acquisition dates t_1 and t_2, and the acquisition dates t_2 and t_3, respectively. Therefore, the double differential vertical displacement ($\Delta DDh_{\perp}$) can be calculated as the double differential vertical bias in the ground range (ΔDD_{gr}) from both image pairs multiplied by $\tan\theta_{inc}$:

$$\Delta DDh_{\perp} = \Delta DD_{gr} * \tan\theta_{inc}, \quad (4)$$

https://doi.org/10.5194/egusphere-2025-603
Preprint. Discussion started: 28 March 2025

The θ_{inc} in radians was generated from the REMA 200 m mosaic DEM based on GAMMA software.

Double-differential vertical displacement maps of PIIS were produced using differential range offset tracking, applied to slant range displacement fields. Ephemeral grounding events were indicated by near-zero displacement in the maps (Figure 3(a)-(c)), resulting in visible 'spots.' These events were also shown in the DInSAR interferogram as a location surrounded by fringes, as pointed out by black arrows in Figure 3(d). Due to coherence loss caused by the rapid movement of the central ice shelf, the ephemeral grounding signal near position L is not visible in the DInSAR interferogram in Figure 3(d). We analyzed each displacement map, noting dates with clear 'spots' at the central PIIS, where the area around Ice rumple L exhibited near-zero displacement (Figure 3(a) and 3(c)). Ephemeral grounding events were compared with double-differential tidal height time series (Figure 4(b)), derived from the CATS2008 ocean tide model (Padman et al., 2002) using Tide Model Driver 3.0 (Greene et al., 2023) at (-75.186576°S, -100.617021°W).

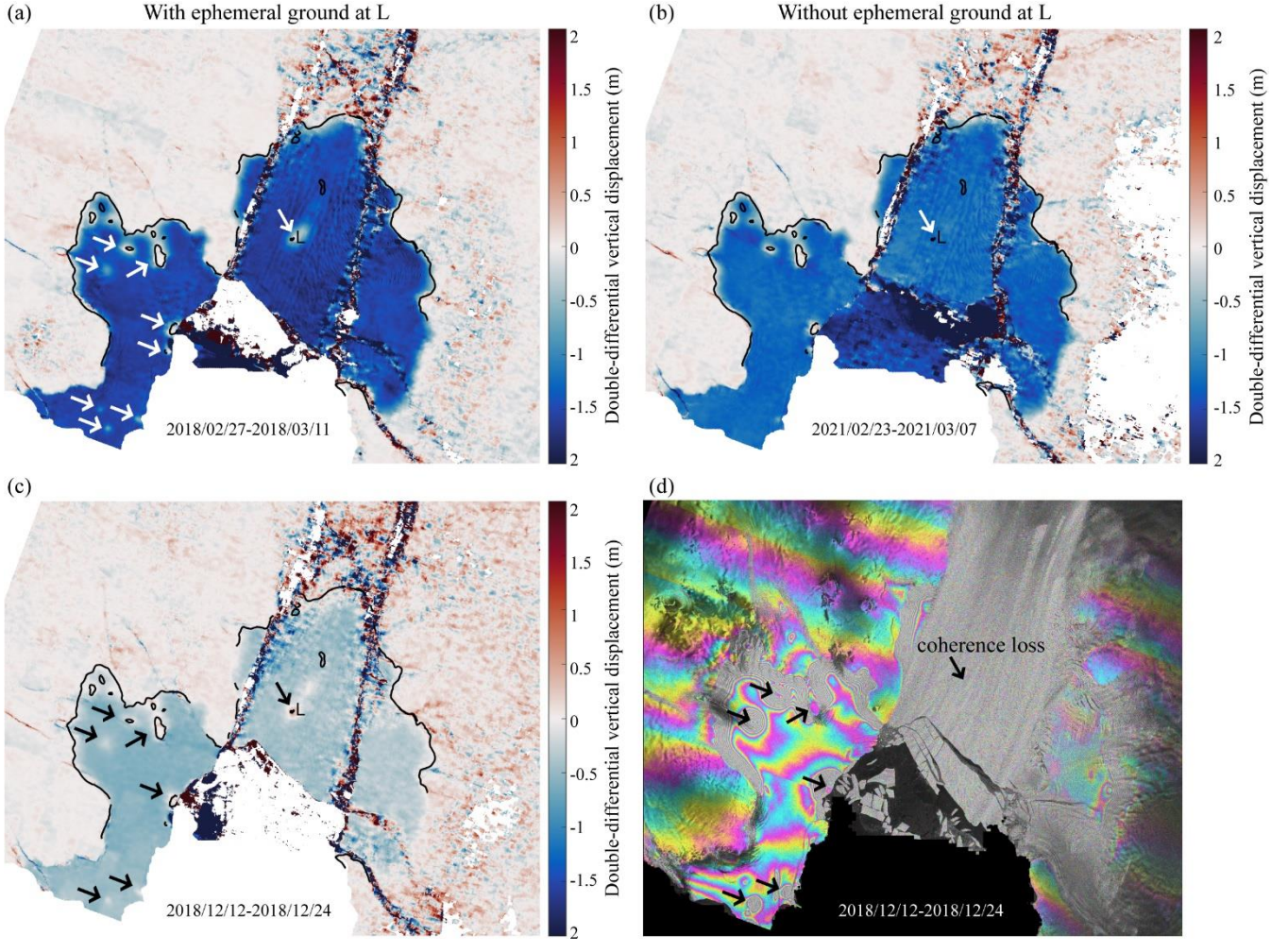

Figure 3. Double-differential vertical displacement compared with DInSAR interferogram, showing ephemeral grounding. (a)Double-differential displacement between 2018/02/27-2018/03/05 and 2018/03/05-2018/03/11. (b) Displacement between 2021/02/23-2021/03/01 and 2021/03/01-2021/03/07. (c) Displacement between 2018/12/12-2018/12/18 and 2018/12/18-2018/12/24. (d) DInSAR interferogram

https://doi.org/10.5194/egusphere-2025-603
Preprint. Discussion started: 28 March 2025

between 2018/12/12-2018/12/18 and 2018/12/18-2018/12/24. White and black arrows highlight the ephemeral grounding location, marked by near-zero displacement. The DInSAR interferogram fails to capture this signal at Ice rumple L due to coherence loss.

2.2 REMA DSM correction

The REMA DSM 2 m strips from October 2010 to December 2022 were corrected by the CryoSat-2 Baseline-D Level 2 SARin product from July 2010 to June 2022 (Meloni et al., 2019) and were coregistered through the code Basal melt rates Using REMA and Google Earth Engine (BURGEE) developed by Zinck et al. (2023a, 2023b). The REMA version 4.1 DSM 2 m strips are 13-year time series of elevation data derived from stereoscopic WorldView and GeoEye satellite imagery acquired from October 2010 to December 2022 (Howat et al., 2022). The DSM strips are referenced to the WGS84 ellipsoid and are not coregistered with satellite altimetry to increase their absolute accuracy. In accordance with Zinck et al. (2023a), the REMA 2 m DEM mosaic created from multiple strips that were coregistered with CryoSat-2 and ICESat (Howat et al., 2019) was used as the reference surface to exclude outliers. Using uncorrected REMA DSM data, we found surface elevation changes at PIIS exceeding 30 m (2010-2022); therefore, we tested elevation differences in the DEM mosaic, setting 100 m as the outlier filter criterion for REMA DSM strips and CryoSat-2 elevations.

We replaced the FES2004 ocean tide model provided by the ESA with the CATS2008 ocean tide model to provide a more accurate ocean loading tide correction value (Zhang et al., 2020). For other corrections, such as solid earth tides, geocentric polar tides, and dry and wet tropospheric and ionospheric effects, we used the data provided by the ESA, as in Zinck et al. (2023a). The erroneous elevation datasets where the interferometric cross-track location failed are filtered based on the quality flags provided by the ESA.

We applied the dynamic and static corrections mentioned in Zinck et al. (2023a) to both the REMA strips and the CryoSat-2 elevations to bring all elevations into the same reference frame regardless of sea level variations. The corrected surface elevation (h) is obtained based on the formula mentioned in Zinck et al. (2023a) as follows:

$$h = h_{Data} - \Delta h_{Geoid} - \alpha(\Delta h_T + \Delta h_{MDT} + \Delta h_{IBE}) \,, \tag{5}$$

where h_{Data} is either the CryoSat-2 or REMA surface elevation above the WGS84 ellipsoid, Δh_{Geoid} is the EGM2008 geoid offset (Pavlis et al., 2012), Δh_T is the tidal height, Δh_{MDT} is the mean dynamic topography, Δh_{IBE} is the inverse barometer effect, and the coefficient α ensures a smooth transition from grounded to floating ice (Shean et al., 2019), which increases from 0 to 1 with distance beyond the grounding line. The grounding line product of the ASAID was used to define α. The correction for the tides and the inverse barometer effect were based on the acquisition time of the first stereo image. The parameter settings for our experiment are the same as the settings mentioned in Zinck et al. (2023a). After this step, both the filtered REMA and CryoSat-2 elevation data are referenced to the EGM2008 geoid.

The double coregistration of the REMA strips was performed based on CryoSat-2 measurements. We have defined the criteria mentioned in Zinck et al. (2023a) that should be fulfilled before the coregistration of a REMA DSM strip with CryoSat-2 data. To include smaller but good-quality REMA strips to obtain a more complete time series of freeboard ice thickness, we set the latitude and longitude criteria for the CryoSat-2 distribution to be at least 5 km for both directions. We

https://doi.org/10.5194/egusphere-2025-603
Preprint. Discussion started: 28 March 2025

set the time gap between the acquisition date of CryoSat-2 and the REMA DSM strip to be within one month, as in Zinck et al. (2023a). Through trial and error, we reset the number of available CryoSat-2 measurements within one month to be at least 75 to ensure that we performed a good plane fit and kept sufficient REMA strips. The residuals between the DEM strips and the median DEM were used to perform the plane fit.

To evaluate the accuracy of the REMA DSM strips, we used four REMA DSM strips from 2019 to 2021 with nearly contemporaneous ICESat-2 elevations (Smith et al., 2024). Using points covered by the REMA DSM strips, the mean elevation difference of the elevation of the REMA DSM strip minus the elevation of the ICESat-2 data was -1.14 m (standard deviation of 2.85 m) over 7285 points in the December 23, 2019 scene, -2.64 m (standard deviation of 1.81 m) over 7837 points in the 11 January 2020 scene, -3.77 m (standard deviation of 2.56 m) over 802 points in the November 24 2021 scene, and -1.93 m (standard deviation of 2.54 m) over a total of 15924 points in four scenes (Table 2). The standard deviations of the elevation of the corrected REMA DSM strips were lower than those of the uncorrected REMA DSM strips. From this comparison, we conclude that the uncertainties for our corrected REMA DSM strips is ±3 m (equivalent to ±24 m in floating ice thickness).

Date	Days Gap (day)	Data	Counts	Mean (m)	Standard deviation (m)
2019/12/23	5	Uncorrected REMA DEM	2335	-5.16	9.34
2019/12/28		Corrected REMA DEM	7285	-1.14	2.85
2020/01/11	2	Uncorrected REMA DEM	6551	0.23	10.11
2020/01/09		Corrected REMA DEM	7837	-2.64	1.81
2021/11/30	6	Uncorrected REMA DEM	827	0.76	5.99
2021/11/24		Corrected REMA DEM	802	-3.77	2.56
Total		Uncorrected REMA DEM	9713	-1.14	10.03
		Corrected REMA DEM	15924	-1.93	2.54

Table 2 The means and standard deviations of uncorrected and corrected REMA DEM strip elevations minus the ICESat-2 elevation

2.3 Ice-equivalent freeboard thickness calculations, surface feature observations and climate data analysis

The ice-equivalent freeboard thickness and Eulerian thickness changes were calculated through the methods provided in Griggs and Bamber (2011) and Shean et al. (2019) based on our corrected REMA DSM 2 m strips, with an ice density of 917 kg/m^3, seawater density of 1027 kg/m^3, and firn air content in meters of ice equivalent derived from the NASA GSFC-FDM v1.2.1 dataset at a 5-day temporal resolution spanning from 1 January 1980 to June 30, 2022 (Medley et al., 2022). We used optical imagery and DSMs to derive surface changes at the PIIS. Surface feature changes at the PIIS were derived from Landsat optical imagery provided by the USGS Earth Explorer and MODIS optical imagery provided in the images of the Antarctic Ice Shelves Version 2 dataset (Scambos et al., 2022) at a spatial resolution of 250 m between 1 January 2001 and 23 October 2023. The surface elevation changes were derived from the corrected REMA DSMs. We used three-month moving mean data from the Oceanic Niño Index (ONI) and year-round monthly mean anomaly data from the Antarctic Oscillation (AAO) index from 2014 to 2023 provided by the Climate Prediction Center to analyze the driving factors behind the appearance of ephemeral grounding events.

https://doi.org/10.5194/egusphere-2025-603
Preprint. Discussion started: 28 March 2025

3 Results

3.1 Changes in the Double-differential Vertical Displacement

Observations of double-differential vertical displacement in the ephemeral grounding zone are influenced by both oceanic tides and ice shelf thinning (Figure 4(a) and Movie S1). This displacement, ranging from -2 m to 2 m closely matching the double-differential tidal height (Figure 4(b)). Positive displacement anomalies correspond to high tidal phases, while negative anomalies correspond to low tidal phases. Figure 4(a) illustrates this relationship, showing the floating region where negative double-differential vertical displacement indicated in blue. Movie S1 provides a more complete visualization, showing both negative and positive displacement. The floating area (exhibiting both negative and positive anomalies) is enclosed by the 2011 grounding line, derived using the DInSAR method. Our results are consistent with Friedl et al. (2020), who found that DROT-derived grounding zones, indicating the landward limit of tidal flexure, were located seaward (up to ~2 km) of those derived from DInSAR. A near-zero vertical displacement signal was observed at ice rumple L from at least 4 November 2016, until the 2020 calving event (11 February 2020), subsequently reappearing on 21 October 2021 (pointed out by red arrow in Figure 4(a) and marked as red circle in Figure 4(b)). Analysis of the ONI time series (Figure 4(c)) reveals three warm periods (2015-2016, 2019, and 2024) and four cold periods (2017, 2018, 2021, and 2022-2023). Concurrently, the AAO index (Figure 4(d)) shows two positive phases during the warm periods (2015-2016 and 2019) and four positive phases during the cold periods (2018, 2021, 2022, and 2023). These coupled atmospheric and oceanic forcings modulate oceanic conditions (Huguenin et al., 2024) and, consequently, the ephemeral grounding behavior.

https://doi.org/10.5194/egusphere-2025-603
Preprint. Discussion started: 28 March 2025

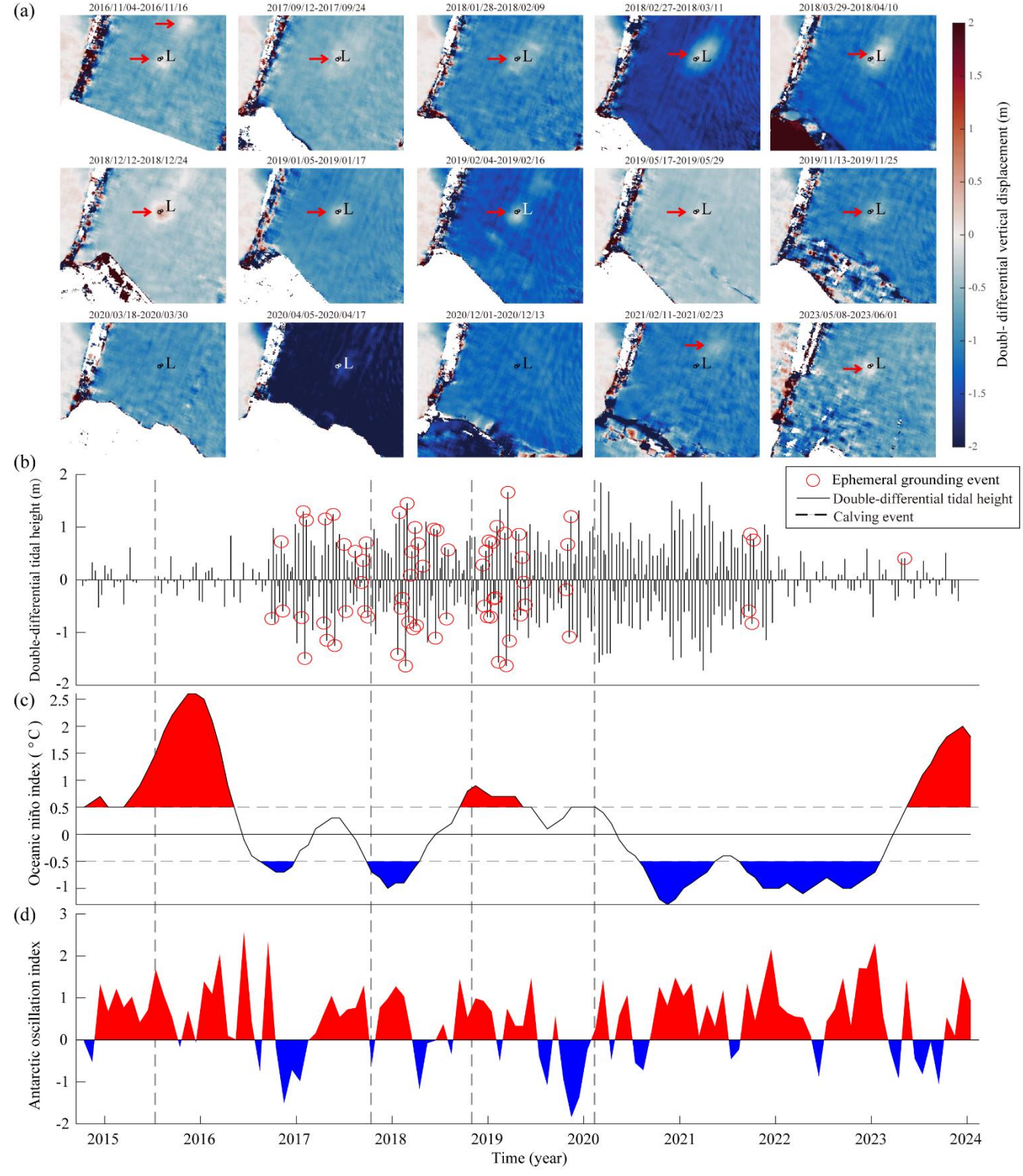

https://doi.org/10.5194/egusphere-2025-603
Preprint. Discussion started: 28 March 2025

Figure 4. 2D double-differential vertical displacement changes, tidal height difference changes, ONI changes, and AAO index changes. (a) Examples of 2D double-differential vertical displacement changes from November 2016 to May 2023. Red arrow point out the ephemeral grounding signal in each result. (b) Time series of double-differential tidal height (black vertical lines) and ephemeral grounding events (red circles). Four dashed lines represent four calving events in 13 July 2015, 12 October 2017, 31 October 2018, and 11 February 2020. (c) Time series of the ONI. Red parts with values above 0.5°C indicate a warm period (El Niñ o),and blue parts with values below -0.5°C indicate a cold period (La Niñ a).(d) Time series of the AAO index. The red parts with values above 0 indicate a positive phase, and the blue parts with values below 0 indicate a negative phase.

3.2 Changes in surface features and ice thickness

The surface features observed from the MODIS images and surface elevations obtained from the corrected REMA DSM in Figure 5 show a surface ridge (~10 km long, ~2.5 km wide, which is circled by an ellipse in Figure 5) formed before 2 December 2010 and advected over the ice rumple L after 2 October 2014. Comparing the changes in surface features with the changes in surface elevation (Figure 6), we determined that the elevation of surface ridges passing through the ice rumple L after 3 October 2019 (<80m) was lower than that in 2015 (>80m). The number of surface ridges increased on 3 October 2019, compared with that before 5 November 2018.

https://doi.org/10.5194/egusphere-2025-603
Preprint. Discussion started: 28 March 2025

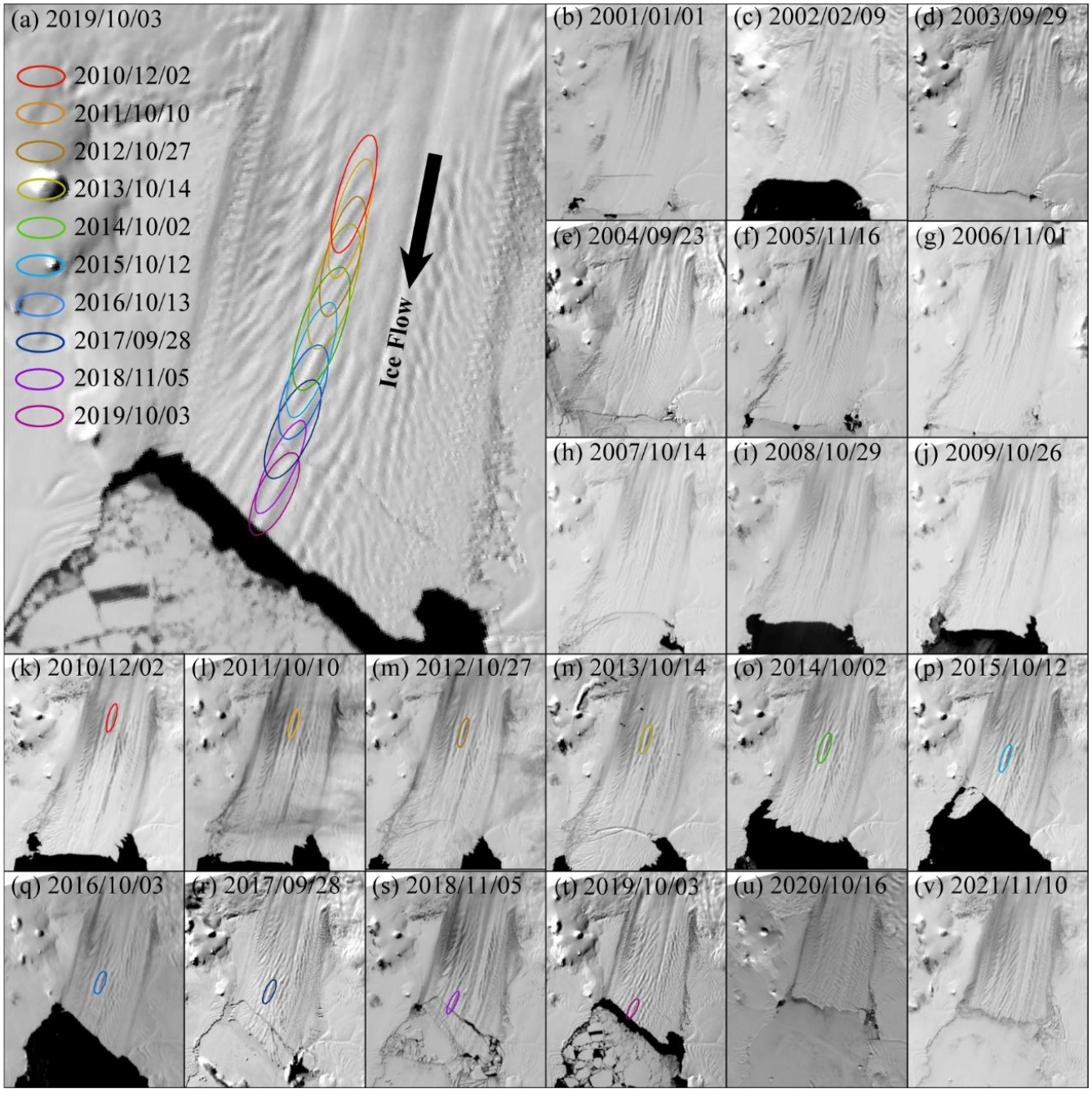

Figure 5. Surface ridge advects with ice flow between 2 December 2010 and 3 October 2019, and surface features change between January 2001 and November 2021. The ellipses with different colors circle a surface ridge that starts existing in (k) and continues advecting downstream. The background images are MODIS images between 1 January 2001 and 3 October 2019.

https://doi.org/10.5194/egusphere-2025-603
Preprint. Discussion started: 28 March 2025

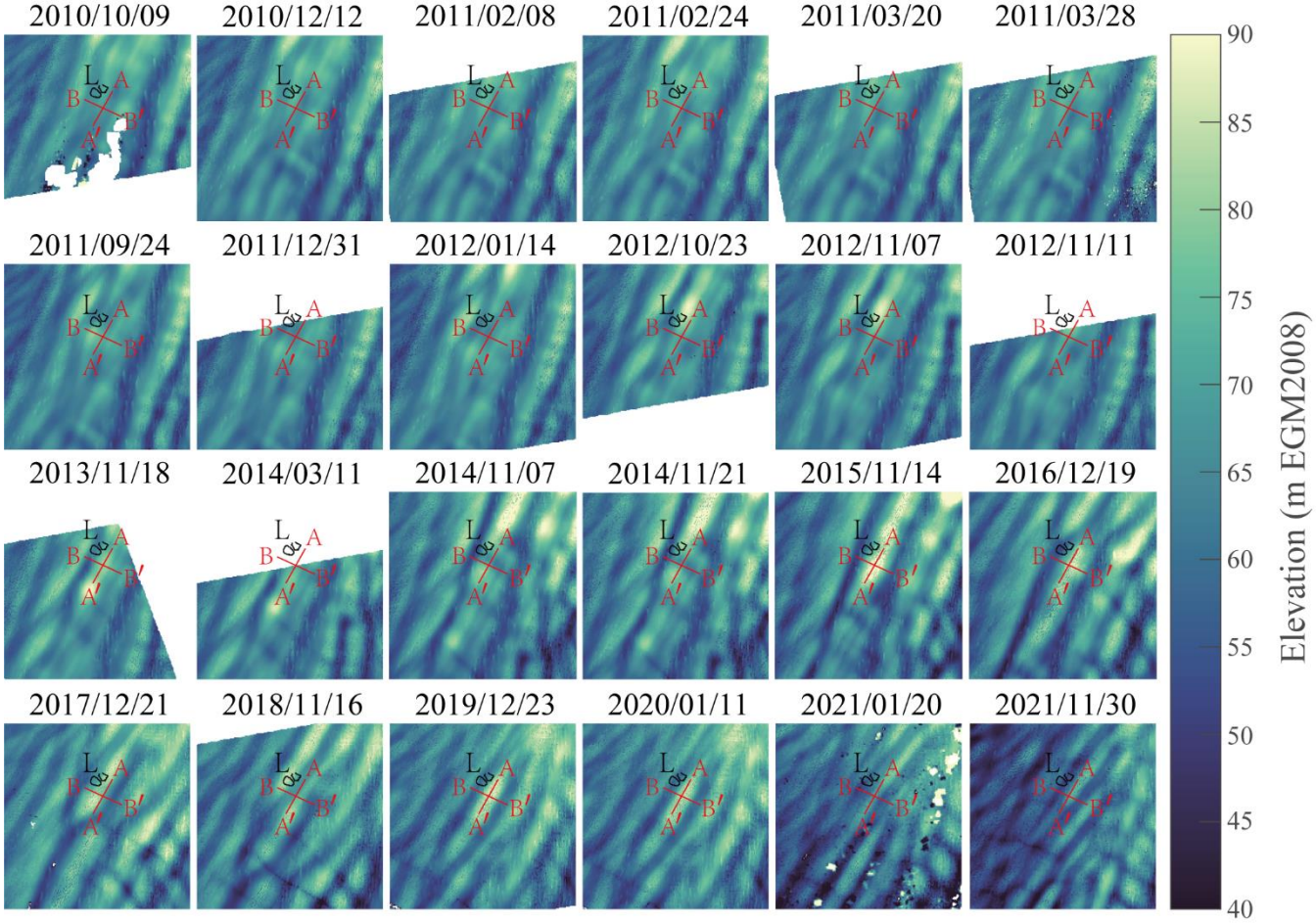

Figure 6. Surface elevation changes near the ice rumple L from 2010 to 2021 derived from corrected REMA DEMs. Lines AA' and BB' are used to extract the ice-equivalent freeboard thickness profiles in Figure 7. The two black circles represent the 2011 grounding lines.

The ice-equivalent freeboard thickness profiles (Figure 7(a)-(c)) provide evidence linking the observed double-differential vertical displacement signals to ephemeral grounding. Figure 7(a) and 7(b) illustrate the ice-equivalent freeboard thickness from 2010 to 2021 along longitudinal profile AA' and transverse profile BB', respectively. The surface elevation differences between 12 December 2010 and the other dates in Figure 7(c) reveal that the ridge on 14 November 2015 was approximately 35 m higher than on 12 December 2010, resulting in increased ice-equivalent freeboard thickness and regrounding of the ice shelf. However, after 11 January 2020, thinner ice advected over the submarine ridge (Figure 7(b)), as evidenced by the reduced surface elevation and the absence of contact between the ice shelf base and the ridge. This transition is consistent with the double-differential vertical displacement time series, where anomalies near ice rumple L diminished significantly after the 2020 calving event (11 February 2020).

https://doi.org/10.5194/egusphere-2025-603
Preprint. Discussion started: 28 March 2025

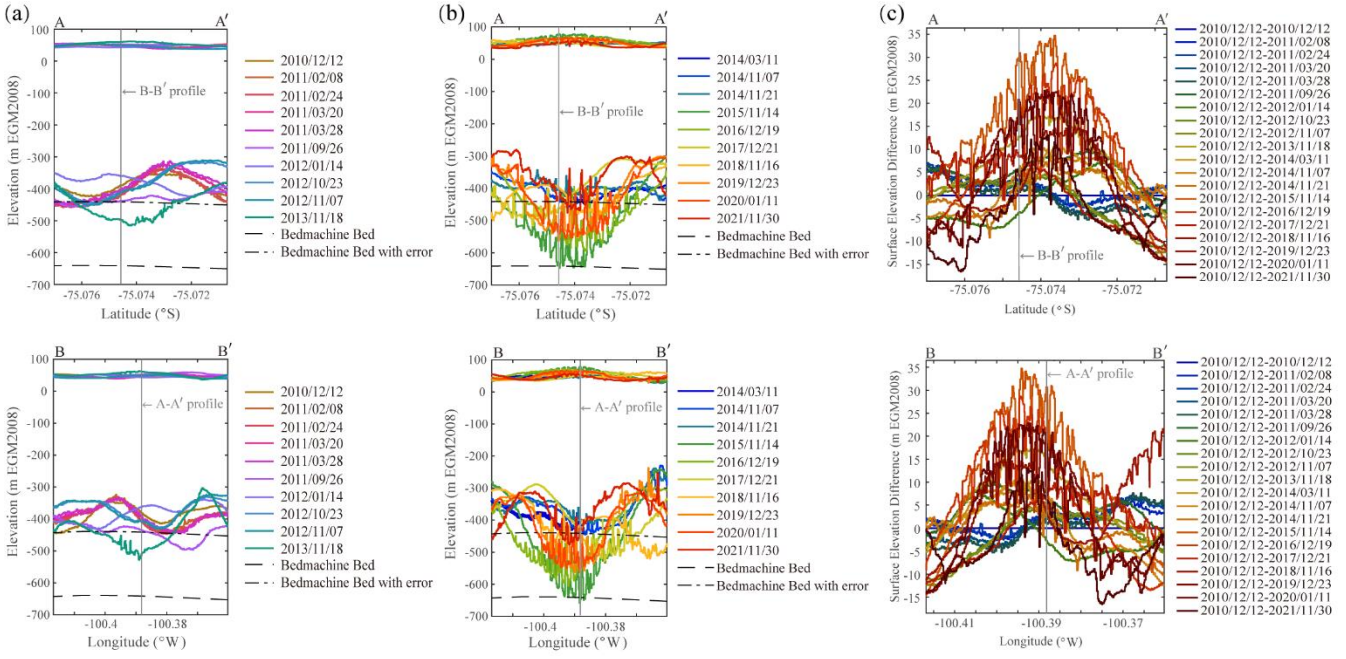

Figure 7. Ice-equivalent freeboard thickness and surface elevation profiles from 2010 to 2021. (a) Elevation profiles along lines AA' and BB' from December 2010 to November 2013. (b) Elevation profiles along line AA' and BB' from March 2014 to November 2021. (c) The surface elevation difference calculated from the surface elevation from other dates minus the elevation on 12 December 2010. The vertical gray line marks the intersection of profiles AA' and BB'. Dashed black lines in (a) and (b) show bed elevations from the BedMachine v3 dataset (Morlighem et al., 2020; Morlighem, 2022). Bed elevations, converted from EIGEN-6C4 to the EGM2008 geoid for consistency with REMA DSM strips, have an estimated error of 200 m.

4 Discussion

Tidal variations can modulate the vertical position of the ice shelf base, causing sub-ice-shelf keels to intermittently contact the seafloor, resulting in ephemeral grounding (Minchew et al., 2017). The vertical height, which is calculated from the double-differential vertical displacement, can simply illustrate the ephemeral grounding location and grounding line location (Figure 4(a), Movie S1). The area changes of the 'spots' near the position L in Figure 4(a) regularly varies from time to time, supporting the evidence that corrugations with periodic spacing on the submarine ridge were caused by sub-ice-shelf keels with tidal modulation (Graham et al., 2013; Davies et al., 2017). Our results show that double-differential vertical displacement can rarely be observed in the ice rumple L after the 2020 calving event (Figure 4(b)). The ice-equivalent freeboard thickness changes also prove that the deep keels no longer contacted the submarine ridge in 2020 (Figure 7(a)~(b)). Double-differential vertical displacement and ice-equivalent freeboard thickness suggest that sub-ice-shelf keels remained grounded on the submarine ridge until the 2020 calving event. After calving, the ice shelf re-advanced, approaching the historical positions of the 2017 and 2018 calving fronts, which allowed for potential re-grounded of sub-ice-shelf keels.

The formation of sub-ice-shelf keels and basal channels has been attributed to melt-related processes, basal topography, and time-varying ice flow dynamics (Bindschadler et al., 2011; Dutrieux et al., 2013; Stanton et al., 2013; Dutrieux et al., 2014a;

https://doi.org/10.5194/egusphere-2025-603
Preprint. Discussion started: 28 March 2025

Joughin et al., 2016). The basal channel and basal keels form at a similar location (Figure 4), which is related to the bed topography. As the ice moves downstream of the grounding line, local surface elevations evolve as the ice approaches hydrostatic equilibrium (Shean, 2016). A local surface low/high in grounded ice indicates a topographic low/high in the bed, forming surface troughs/ridges (Joughin et al., 2016). The bed topography near the grounding line is W shaped, with two troughs adjacent to the topographic high. These two troughs could allow thicker ice to be advected downstream over the submarine ridge and form surface ridges.

Melt-related processes are also very important for the formation of sub-ice-shelf keels. Based on previous studies, mooring observations over the period from 2009 to 2020 indicate fluctuations in ocean temperature variability (Christianson et al, 2016; Joughin et al., 2021). From 2009 to 2017, the basal melt rate of the PIIS decreased (Paolo et al., 2023). From 2012 to 2014, atmospheric teleconnection caused by a La Niña event weakened CDW advection from the open ocean, cooled the PIB, and decreased basal melt rates (Thoma et al., 2008; Dutrieux et al., 2014b; St-Laurent et al., 2015; Christianson et al., 2016; Webber et al., 2017; Davis et al., 2018; Liu et al., 2024; Huguenin et al., 2024). This is because El Niño weakens coastal easterlies and enhances the cross-shelf transport of warm CDW, whereas La Niña allows stronger surface easterlies and increases the on-shelf flow of cold surface waters, which reduces the cross-shelf transport of warm CDW (Huguenin et al., 2024). Mooring observations revealed no evident changes in ocean temperature time series from 2017 to 2020 (Joughin et al., 2021). The meltwater flux from the PIG in 2020 was approximately half that in 2009 and equivalent to that in 2012 and 2014 (Yoon et al., 2022). Additionally, there was a significant decreasing trend in the wind speed and deep seawater temperature at depths ranging from 880 m to 1000 m near the ice front between 2015 and 2018 (Liu et al., 2024). The ONI time series indicates that a strong El Niño started in 2015, followed by two weak La Niña events in 2017 and 2018 and a weak El Niño event in 2019 (Figure 3(c)). In general, positive phases of the SAM are more likely to occur during La Niña, whereas negative phases occur more frequently during El Niño. However, two positive phase periods of the AAO appeared in 2015 and 2019 during the two El Niño events (Figure 3(d)). Huguenin et al. (2024) noted that the AAO tends to offset the ENSO warming effect and reduce the strength of the atmospheric teleconnection to the Amundsen Sea region. Combining the ONI and AAO time series with ocean conditions from 2015 to 2020, we can infer that basal melting was weak during the cold period from 2015 to 2020 and may have allowed thicker ice to advect farther downstream, causing ephemeral grounding at the submarine ridge until the 2020 calving event.

As mentioned by Bradley et al. (2022), when the ice front of the PIG retreated from the 2009 position to the 2020 position, melt rates within 10 km of the ice front increased significantly; the melt response to calving was sensitive to the thickness of the gap between the ice shelf and the seabed ridge. As shown by our ice thickness results (Figure 6(b)), the ice thickness decreased significantly between 11 January 2020 and 20 November 2021. This implies that the ice shelf becomes thinner and that the thickness gap between the ice shelf and the submarine ridge becomes larger, resulting in a higher basal melting rate. Because of the thinner ice thickness and the higher basal melting rate, the ephemeral grounding signals disappeared after the 2020 calving event.

https://doi.org/10.5194/egusphere-2025-603
Preprint. Discussion started: 28 March 2025

Based on the time series surface changes in the PIIS, we agree with Joughin et al. (2021), who proposed that ephemeral grounding may be related to some of the transverse rifts that originated south of the ice rumple L and caused the four calving events that occurred between 2015 and 2020. However, the unclear pattern of newly formed rifts in SAR imagery limits the ability to investigate how ephemeral grounding influences rift formation. Furthermore, Arndt et al. (2018) reported that the final pinning points are important controls on the orientation of the calving line of the PIIS. We propose that the ephemeral grounding site at the central ice shelf may evolve into a final pinning point after the 2015 calving event and influenced rift propagation, which led to future ice shelf calving events in 2017, 2018, and 2020. Further studies on ice shelf modeling are needed to understand how the ephemeral grounding site on the central PIIS influences rift propagation.

5 Conclusions

This study used double-differential vertical displacement time series observations from Sentinel-1A/B imagery to identify a pattern in ephemeral grounding changes between October 2014 and December 2023. We found that the ephemeral grounding site on the central ice shelf of the PIIS appeared until the 2020 calving event and after October 2021. The double-differential vertical displacement time series support the evidence that the periodically spaced corrugations on the submarine ridge are caused by sub-ice-shelf keels with tidal modulation. Based on our observations and previous studies, we conclude that the decrease in basal melting due to La Niña and the positive phase of AAO allowed thicker ice to move over the submarine ridge and cause ephemeral grounding. However, the 2020 calving event increased the basal melting rate outside of the submarine ridge and caused the ephemeral grounding to disappear. We conclude that calving and atmospheric forcing influence basal melting and indirectly influence ephemeral grounding. We propose that the ephemeral grounding site at the central ice shelf may evolve into a final pinning point and may influence future ice shelf calving events. Further studies on ice shelf modeling are needed to understand the interaction between ephemeral grounding and rift propagation.

***Code and sample availability*:** All codes and processed time series data used for analysis and plotting in this study are available from Qian et al. (2025a), including ice front positions delineated from Landsat panchromatic imagery and Sentinel-1 SAR imagery based on Google Earth Engine, double-differential vertical displacement, and corrected REMA DSM strips. The zenodo link provided in Qian et al. (2025a) will be made public after acceptance of the paper.

Data availability: All software (except GAMMA, which is commercial software), codes, and satellite and climate datasets used in this study are publicly available and can be obtained from the following sources: The MATLAB plotting codes on which this article is based are available in Greene et al (2017) and Greene et al. (2021). The BURGEE codes for corrected REMA DSM strips are available in Zinck et al. (2023b). The tidal model driver based on MATLAB code is available in Greene et al. (2023). Sentinel-1 images are available for free download from the Alaska Satellite Facility website at https://asf.alaska.edu/. Processed MODIS images are available in Scambos et al. (2022). BedMachine version 3 dataset is from Morlighem (2022). REMA DSM 200 m mosaic and REMA DSM 2 m strips are available from Howat et al. (2022a) and Howat et al. (2022b), respectively. CryoSat Baseline-D SARIn Level 2 data are available on the ESA CryoSat Science Server at https://science-pds.cryosat.esa.int/#Cry0Sat2_data%2FIce_Baseline_D%2FSIR_SIN_L2. ICEsat-2 Level 2 ATL06 product is available from Smith et al. (2023). Ground line products are available from Rignot et al. (2016), Floricioiu et al. (2021), and Mohajerani et al. (2021). Firn air content is available from Medley et al. (2022). Single-level hourly ERA5 data

https://doi.org/10.5194/egusphere-2025-603
Preprint. Discussion started: 28 March 2025

from 1940 to present are available from Hersbach et al. (2023). The Oceanic Niño Index and the Antarctic Oscillation Index are available from the National Oceanic and Atmospheric Administration (NOAA) Climate Prediction Center at https://origin.cpc.ncep.noaa.gov/products/analysis_monitoring/ensostuff/ ONI_v5.php and https://www.cpc.ncep.noaa.gov/products/precip/CWlink/daily_ao_index/aao/monthly.aao.index.b79.current.ascii, respectively.

Video supplement: Movie S1 "Double-differential vertical displacement changes from November 2014 to November 2023 at the PIIS" can be accessed at the zenodo link provide by Qian et al. (2025b).

Author contribution: YQ and CZ designed the experiments and YQ carried them out. YQ developed the MATLAB code and performed all the experiments. BZ provide the corrected CryoSat-2 dataset. YQ prepared the manuscript with contributions from all co-authors.

Competing interests: The contact author has declared that none of the authors has any competing interests.

Acknowledgements: This research is funded by the National Natural Science Foundation of China (41941010 and 42171133) and the Fundamental Research Funds for the Central Universities (2042024kf0016). We thank all the organizations or projects listed in Open Research. We thank the anonymous reviewers and editors for their insightful comments to improve the manuscript. We sincerely thank Anne Solgaard and Anders Kusk for providing helpful suggestions related to SAR image post-processing. We sincerely thank Jan Wuite for providing helpful suggestions related to tidal correction. We sincerely thank Hilmar Gudmundsson for providing helpful suggestions related to the ephemeral grounding change analysis.

Financial support: This research is funded by the National Natural Science Foundation of China (41941010 and 42171133) and the Fundamental Research Funds for the Central Universities (2042024kf0016).

References

Alley, R. B., Anandakrishnan, S., Christianson, K., Horgan, H. J., Muto, A., Parizek, B. R., Pollard, D., and Walker, R. T.: Oceanic forcing of ice-sheet retreat: West Antarctica and more, Annu. Rev. Earth Planet. Sci., 43, 207–231, https://doi.org/10.1146/annurev-earth-060614-105344, 2015.

Arndt, J. E., Larter, R. D., Friedl, P., Gohl, K., Höppner, K., and the Science Team of Expedition PS104: Bathymetric controls on calving processes at Pine Island Glacier, The Cryosphere, 12, 2039–2050, https://doi.org/10.5194/tc-12-2039-2018, 2018.

Bamber, J. L., Westaway, R. M., Marzeion, B., and Wouters, B.: The land ice contribution to sea level during the satellite era, Environ. Res. Lett., 13, 063008, https://doi.org/10.1088/1748-9326/aac2f0, 2018.

Bindschadler, R. A., Vaughan, D. G., and Vornberger, P.: Variability of basal melt beneath the Pine Island Glacier ice shelf, West Antarctica, J. Glaciol., 57, 581–595, https://doi.org/10.3189/002214311797409802, 2011.

https://doi.org/10.5194/egusphere-2025-603
Preprint. Discussion started: 28 March 2025

Boncori, M. J. P., Andersen, M. L., Dall, J., Kusk, A., Martijn, K., Bech Andersen, S., et al.: Intercomparison and validation of SAR-based ice velocity measurement techniques within the Greenland ice sheet cci project, Remote Sens., 10, 929, https://doi.org/10.3390/rs10060929, 2018.

Bradley, A. T., Bett, D. T., Dutrieux, P., De Rydt, J., and Holland, P. R.: The influence of Pine Island Ice Shelf calving on basal melting, J. Geophys. Res. Oceans, 127, e2022JC018621, https://doi.org/10.1029/2022JC018621, 2022.

Chen, Y., Zhou, C., Ai, S., Liang, Q., Zheng, L., Liu, R., and Lei, H.: Dynamics of Dålk glacier in east Antarctica derived from multisource satellite observations since 2000, Remote Sens., 12, 1809, https://doi.org/10.3390/rs12111809, 2020.

Christianson, K., Bushuk, M., Dutrieux, P., Parizek, B. R., Joughin, I. R., Alley, R. B., et al.: Sensitivity of Pine Island Glacier to observed ocean forcing, Geophys. Res. Lett., 43, 10817–10825, https://doi.org/10.1002/2016GL070500, 2016.

Davies, D., Bingham, R. G., Graham, A. G. C., Spagnolo, M., Dutrieux, P., Vaughan, D. G., et al.: High-resolution subb-ice-shelf seafloor records of twentieth century ungrounding and retreat of Pine Island Glacier, West Antarctica, J. Geophys. Res. Earth Surf., 122, 1698–1714, https://doi.org/10.1002/2017JF004311, 2017.

Davis, P. E. D., Jenkins, A., Nicholls, K. W., Brennan, P. V., Abrahamsen, E. P., Heywood, K. J., et al.: Variability in basal melting beneath Pine Island Ice Shelf on weekly to monthly timescales, J. Geophys. Res. Oceans, 123, 8655–8669, https://doi.org/10.1029/2018JC014464, 2018.

Dutrieux, P., Stewart, C., Jenkins, A., Nicholls, K. W., Corr, H. F. J., Rignot, E., and Steffen, K.: Basal terraces on melting ice shelves, Geophys. Res. Lett., 41, 5506–5513, https://doi.org/10.1002/2014GL060618, 2014a.

Dutrieux, P., Rydt, J. D., Jenkins, A., Holland, P. R., Ha, H. K., Lee, S. H., et al.: Strong sensitivity of pine island ice-shelf melting to climatic variability, Science, 343, 174–178, https://doi.org/10.1126/science.1244341, 2014b.

Dutrieux, P., Vaughan, D. G., Corr, H. F. J., Jenkins, A., Holland, P. R., Joughin, I., and Fleming, A. H.: Pine Island glacier ice shelf melt distributed at kilometre scales, The Cryosphere, 7, 1543–1555, https://doi.org/10.5194/tc-7-1543-2013, 2013.

Floricioiu, D., Krieger, L., Chowdhury, T. A., and Bässler, M.: ESA Antarctic Ice Sheet Climate Change Initiative (Antarctic_Ice_Sheet_cci): Grounding line location for key glaciers, Antarctica, 1994–2020, Version 2, ERC EDS Centre for Environmental Data Analysis, https://catalogue.ceda.ac.uk/uuid/7b3bddd5af4945c2ac508a6d25537f0a/, 2021.

Fricker, H. A., and Padman, L.: Ice shelf grounding zone structure from ICESat laser altimetry, Geophys. Res. Lett., 33, L15502, https://doi.org/10.1029/2006GL026907, 2006.

Fried, M. J., Hulbe, C. L., and Fahnestock, M. A.: Grounding-line dynamics and margin lakes, Ann. Glaciol., 55, 87–96, https://doi.org/10.3189/2014AoG66A216, 2014.

Friedl, P., Weiser, F., Fluhrer, A., and Braun, M. H.: Remote sensing of glacier and ice sheet grounding lines: A review, Earth-Sci. Rev., 201, 102948, https://doi.org/10.1016/j.earscirev.2019.102948, 2020.

Fürst, J., Durand, G., Gillet-Chaulet, F., Tavard, L., Rankl, M., Braun, M., and Gagliardini, O.: The safety band of Antarctic ice shelves, Nat. Clim. Change, 6, 479–482, https://doi.org/10.1038/nclimate2912, 2016.

Gudmundsson, G. H., Paolo, F. S., and Adusumilli, S., Fricker, H. A.: Instantaneous Antarctic ice sheet mass loss driven by thinning ice shelves, Geophys. Res. Lett., 46, 13903–13909, https://doi.org/10.1029/2019GL085027, 2019.

https://doi.org/10.5194/egusphere-2025-603
Preprint. Discussion started: 28 March 2025

Graham, A. G. C., Dutrieux, P., Vaughan, D. G., Nitsche, F. O., Gyllencreutz, R., Greenwood, S. L., et al.: Seabed corrugations beneath an Antarctic ice shelf revealed by autonomous underwater vehicle survey: Origin and implications for the history of pine island glacier, J. Geophys. Res. Earth Surf., 118, 1356–1366, 2013

Greene, C. A., Gwyther, D. E., and Blankenship, D. D.: Antarctic mapping tools for MATLAB, Comput. Geosci., 104, 151–157, https://doi.org/10.1016/j.cageo.2016.08.003, 2017.

Greene, C. A.: Antarctic Mapping Tools, Version 6, [Software], GitHub, https://github.com/chadagreene/Antarctic-Mapping-Tools, 2021.

Greene, C. A., Erofeeva, S., Padman, L., Howard, S., Sutterley, T., and Egbert, G.: The Tide Model Driver for MATLAB, Version 3.0, [Software], https://github.com/chadagreene/Tide-Model-Driver, 2023.

Griggs, J. A. and Bamber, J. L.: Antarctic ice-shelf thickness from satellite radar altimetry, J. Glaciol., 57, 485–498, https://doi.org/10.3189/002214311796905659, 2011.

Hillenbrand, C. D., Smith, J. A., Hodell, D. A., Greaves, M., Poole, C. R., Kender, S., et al.: West Antarctic ice sheet retreat driven by Holocene warm water incursions, Nature, 547, 43–48, https://doi.org/10.1038/nature22995, 2017.

Hogg, A. E.: Locating Ice Sheet Grounding Lines Using Satellite Radar Interferometry and Altimetry, PhD Thesis, University of Leeds, 152 pp., https://etheses.whiterose.ac.uk/11356/, 2015.

Howat, I., Porter, C., Smith, B. E., Noh, M. J., and Morin, P.: The reference elevation model of Antarctica, The Cryosphere, 13, 665–674, https://doi.org/10.5194/tc-13-665-2019, 2019.

Howat, I., Porter, C., Noh, M., Husby, E., Khuvis, S., Danish, E., et al.: The Reference Elevation Model of Antarctica – Strips, Version 4.1, [Dataset], Harvard Dataverse, https://data.pgc.umn.edu/elev/dem/setsm/REMA/strips/s2s041/2m/s76w101/, 2022a.

Howat, I., Porter, C., Noh, M., Husby, E., Khuvis, S., Danish, E., et al.: The Reference Elevation Model of Antarctica – Mosaics, Version 1.1, [Dataset], Harvard Dataverse, https://data.pgc.umn.edu/elev/dem/setsm/REMA/mosaic/v1.1/200m/, 2022b.

Huguenin, M. F., Holmes, R. M., Spence, P., and England, M. H.: Subsurface warming of the West Antarctic continental shelf linked to El Niño-Southern Oscillation, Geophys. Res. Lett., 51, e2023GL104518, https://doi.org/10.1029/2023GL104518, 2024.

Jacobs, S. S., Jenkins, A., Giulivi, C. F., and Dutrieux, P.: Stronger ocean circulation and increased melting under pine island glacier ice shelf, Nat. Geosci., 4, 519–523, https://doi.org/10.1038/ngeo1188, 2011.

Jenkins, A., Dutrieux, P., Jacobs, S. S., McPhail, S. D., Perrett, J. R., Webb, A. T., and David, W.: Observations beneath pine island glacier in west Antarctica and implications for its retreat, Nat. Geosci., 3, 468–472, https://doi.org/10.1038/ngeo890, 2010.

Jeong, S., Howat, I. M., and Bassis, J. N.: Accelerated ice shelf rifting and retreat at pine island glacier, west Antarctica, Geophys. Res. Lett., 43, 11720–11725, https://doi.org/10.1002/2016GL071360, 2016.

https://doi.org/10.5194/egusphere-2025-603
Preprint. Discussion started: 28 March 2025

Joughin, I., Shapero, D., Smith, B., Dutrieux, P., and Barham, M.: Ice-shelf retreat drives recent pine island glacier speedup, Sci. Adv., 7, eabg3080, https://doi.org/10.1126/sciadv.abg3080, 2021.

Joughin, I., Shean, D. E., Smith, B. E., and Dutrieux, P.: Grounding line variability and subglacial lake drainage on pine island glacier, Antarctica, Geophys. Res. Lett., 43, 9093–9102, https://doi.org/10.1002/2016GL070259, 2016.

Joughin, I., Smith, B. E., and Abdalati, W.: Glaciological advances made with interferometric synthetic aperture radar, J. Glaciol., 56, 1026–1042, https://doi.org/10.3189/002214311796406158, 2010.

Lemos, A., Shepherd, A., McMillan, M., Hogg, A. E., Hatton, E., and Joughin, I.: Ice velocity of Jakobshavn Isbræ, Petermann Glacier, Nioghalvfjerdsfjorden, and Zachariæ Isstrøm, 2015–2017, from Sentinel-1A/B SAR imagery, The Cryosphere, 12, 2087–2097, https://doi.org/10.5194/tc-12-2087-2018, 2018.

Lei, Y., Gardner, A., and Agram, P.: Autonomous repeat image feature tracking (autorift) and its application for tracking ice displacement, Remote Sens., 13, 749, https://doi.org/10.3390/rs13040749, 2021.

Liu, M., Wang, Z., Zhang, B., Song, X., and An, J.: The variation in basal channels and basal melt rates of Pine Island Ice Shelf, Acta Oceanol. Sin., 43, 22–34, https://doi.org/10.1007/s13131-023-2271-x, 2024.

Marsh, O. J., Rack, W., Floricioiu, D., Golledge, N. R., and Lawson, W.: Tidally induced velocity variations of the Beardmore Glacier, Antarctica, and their representation in satellite measurements of ice velocity, The Cryosphere, 7, 1375–1384, https://doi.org/10.5194/tc-7-1375-2013, 2013.

Meloni, M., Bouffard, J., Parrinello, T., Dawson, G., Garnier, F., Helm, V., et al.: CryoSat Ice Baseline-D Validation and Evolutions, The Cryosphere, 14, 1889–1907, https://doi.org/10.5194/tc-14-1889-2020, 2020.

Medley, B., Neumann, T. A., Zwally, H. J., Smith, B. E., and Stevens, C. M.: Simulations of firn processes over the Greenland and Antarctic ice sheets: 1980–2021, The Cryosphere, 16, 3971–4011, https://doi.org/10.5194/tc-16-3971-2022, 2022a.

Medley, B., Neumann, T. A., Zwally, H. J., Smith, B. E., and Stevens, C. M.: NASA GSFC Firn Densification Model version 1.2.1 (GSFC-FDMv1.2.1) for the Greenland and Antarctic Ice Sheets: 1980–2022, Version 1.2.1, [Dataset], Zenodo, https://zenodo.org/records/7221954, 2022b.

Miles, B. W. J. and Bingham, R. G.: Progressive unanchoring of Antarctic ice shelves since 1973, Nature, 626, 785–791, https://doi.org/10.1038/s41586-024-07049-0, 2024.

Milillo, P., Rignot, E., Mouginot, J., Scheuchl, B., Morlighem, M., Li, X., and Salzer, J. T.: On the short-term grounding zone dynamics of Pine Island Glacier, West Antarctica, observed with COSMO-SkyMed interferometric data, Geophys. Res. Lett., 44, 10436, https://doi.org/10.1002/2017GL074811, 2017.

Milillo, P., Rignot, E., Rizzoli, P., Scheuchl, B., Mouginot, J., Bueso-Bello, J., and Prats-Iraola, P.: Heterogeneous retreat and ice melt of Thwaites Glacier, West Antarctica, Sci. Adv., 5, aau3433, https://doi.org/10.1126/sciadv.aau3433, 2019.

Minchew, B. M., Simons, M., Riel, B., and Milillo, P.: Tidally induced variations in vertical and horizontal motion on Rutford ice stream, west Antarctica, inferred from remotely sensed observations, J. Geophys. Res. Earth Surf., 122, 167–190, https://doi.org/10.1002/2016JF003971, 2017.

https://doi.org/10.5194/egusphere-2025-603
Preprint. Discussion started: 28 March 2025

Mohajerani, Y., Jeong, S., Scheuchl, B., Velicogna, I., Rignot, E., and Milillo, P.: Automatic delineation of glacier grounding lines in differential interferometric synthetic-aperture radar data using deep learning, Sci. Rep., 11, 4992, https://doi.org/10.1038/s41598-021-84309-3, 2021.

Morlighem, M., Rignot, E., Binder, T., Blankenship, D., Drews, R., Eagles, G., et al.: Deep glacial troughs and stabilizing ridges unveiled beneath the margins of the Antarctic ice sheet, Nat. Geosci., 13, 132–137, https://doi.org/10.1038/s41561-019-0510-8, 2020.

Morlighem, M.: MEaSUREs BedMachine Antarctica, Version 3, [Dataset], NASA National Snow and Ice Data Center Distributed Active Archive Center, https://nsidc.org/data/nsidc-0756/versions/3, 2022.

Paolo, F. S., Gardner, A. S., Greene, C. A., Nilsson, J., Schodlok, M. P., Schlegel, N.-J., and Fricker, H. A.: Widespread slowdown in thinning rates of West Antarctic ice shelves, The Cryosphere, 17, 3409–3433, https://doi.org/10.5194/tc-17-3409-2023, 2023.

Paul, F., Bolch, T., Kääb, A., Nagler, T., Nuth, C., Scharrer, K., et al.: The glaciers climate change initiative: Methods for creating glacier area, elevation change and velocity products, Remote Sens. Environ., 162, 408–426, https://doi.org/10.1016/j.rse.2013.07.043, 2015.

Pavlis, N. K., Holmes, S. A., Kenyon, S. C., and Factor, J. K.: The development and evaluation of the Earth Gravitational Model 2008 (EGM2008), J. Geophys. Res., 117, B04406, https://doi.org/10.1029/2011JB008916, 2012.

Pritchard, H. D., Ligtenberg, S. R. M., Fricker, H. A., Vaughan, D. G., van den Broeke, M. R., and Padman, L.: Antarctic ice-sheet loss driven by basal melting of ice shelves, Nature, 484, 502–505, https://doi.org/10.1038/nature10968, 2012.

Qi, M., Liu, Y., Liu, J., Cheng, X., Lin, Y., Feng, Q., et al.: A 15-year circum-Antarctic iceberg calving dataset derived from continuous satellite observations, Earth Syst. Sci. Data, 13, 4583–4601, https://doi.org/10.5194/essd-13-4583-2021, 2021.

Qian, Y. D.: Dataset for the paper "Ephemeral grounding on the Pine Island Ice Shelf, West Antarctica, from 2014 to 2023", Version 5, Zenodo, https://doi.org/10.5281/zenodo.13357909, 2025a.

Qian, Y. D.: Double-differential vertical displacement changes from November 2014 to November 2023 at the Pine Island Ice Shelf., Version 1, Zenodo, https://zenodo.org/records/14843806, 2025b.

Rignot, E.: Fast Recession of a West Antarctic Glacier, Science, 281, 549–551, https://doi.org/10.1126/science.281.5376.549, 1998.

Rignot, E.: Ice-shelf changes in pine island bay, Antarctica, 1947–2000, J. Glaciol., 48, 247–256, https://doi.org/10.3189/172756502781831386, 2002.

Rignot, E., Casassa, G., Gogineni, P., Krabill, W., Rivera, A., and Thomas, R.: Accelerated ice discharge from the Antarctic Peninsula following the collapse of Larsen B Ice Shelf, Geophys. Res. Lett., 31, L18401, https://doi.org/10.1029/2004GL020697, 2004.

Rignot, E., Mouginot, J., Morlighem, M., Seroussi, H., and Scheuchl, B.: Widespread, rapid grounding line retreat of Pine Island, Thwaites, Smith, and Kohler Glaciers, West Antarctica, from 1992 to 2011, Geophys. Res. Lett., 41, 3502–3509, https://doi.org/10.1002/2014GL060140, 2014.

https://doi.org/10.5194/egusphere-2025-603
Preprint. Discussion started: 28 March 2025

Rignot, E., Mouginot, J., and Scheuchl, B.: Measures Antarctic grounding line from differential satellite radar interferometry, Version 2, [Dataset], NASA National Snow and Ice Data Center Distributed Active Archive Center, https://nsidc.org/data/NSIDC-0498/versions/2, 2016.

Rott, H., Rack, W., Skvarca, P., and De Angelis, H.: Northern Larsen Ice Shelf, Antarctica: Further retreat after collapse, Ann. Glaciol., 34, 277–282, 2002.

Rott, H., Abdel Jaber, W., Wuite, J., Scheiblauer, S., Floricioiu, D., van Wessem, J. M., et al.: Changing pattern of ice flow and mass balance for glaciers discharging into the Larsen A and B embayments, Antarctic Peninsula, 2011 to 2016, The Cryosphere, 12, 1273–1291, https://doi.org/10.5194/tc-12-1273-2018, 2018.

Sánchez-Gámez, P. and Navarro, F. J.: Glacier surface velocity retrieval using D-InSAR and offset tracking techniques applied to ascending and descending passes of sentinel-1 data for southern Ellesmere ice caps, Canadian Arctic, Remote Sens., 9, 442, https://doi.org/10.3390/rs9050442, 2017.

Scambos, T., Wallin, B., and Bohlander, J.: Images of Antarctic Ice Shelves, Version 2, [Dataset], NASA National Snow and Ice Data Center Distributed Active Archive Center, https://nsidc.org/data/nsidc-0102/versions/2, 2022.

Schmeltz, M., Rignot, E., and MacAyeal, D. R.: Ephemeral grounding as a signal of ice-shelf change, J. Glaciol., 47, 71–77, https://doi.org/10.3189/172756501781832502, 2001.

Scheuchl, B., Mouginot, J., Rignot, E., Morlighem, M., and Khazendar, A.: Grounding line retreat of Pope, Smith, and Kohler Glaciers, West Antarctica, measured with Sentinel-1a radar interferometry data, Geophys. Res. Lett., 43, 8572–8579, https://doi.org/10.1002/2016GL069287, 2016.

Shean, D. E.: Quantifying ice-shelf basal melt and ice-stream dynamics using high-resolution DEM and GPS time series, PhD Thesis, University of Washington, 2016.

Shean, D. E., Joughin, I. R., Dutrieux, P., Smith, B. E., and Berthier, E.: Ice shelf basal melt rates from a high-resolution digital elevation model (DEM) record for pine island glacier, Antarctica, The Cryosphere, 13, 2633–2656, https://doi.org/10.5194/tc-13-2633-2019, 2019.

Shepherd, A., Ivins, E. R., Geruo, A., Barletta, V. R., Bentley, M. J., Bettadpur, S., et al.: A reconciled estimate of ice-sheet mass balance, Science, 338, 1183–1189, https://doi.org/10.1126/science.1228102, 2012.

Smith, B., Fricker, H. A., Gardner, A. S., Medley, B., Nilsson, J., Paolo, F. S., et al.: Pervasive ice sheet mass loss reflects competing ocean and atmosphere processes, Science, 368, 1239–1242, https://doi.org/10.1126/science.aaz5845, 2020.

Smith, B., Adusumilli, S., Csathó, B. M., Felikson, D., Fricker, H. A., Gardner, A., Holschuh, N., et al.: ATLAS/ICESat-2 L3A Land Ice Height, Version 6, [Dataset], NASA National Snow and Ice Data Center Distributed Active Archive Center, https://doi.org/10.5067/ATLAS/ATL06.006, 2023.

Smith, J. A., Andersen, T. J., Shortt, M., Gaffney, A. M., Truffer, M., Stanton, T. P., et al.: Subb-ice-shelf sediments record history of twentieth-century retreat of pine island glacier, Nature, 541, 77–80, https://doi.org/10.1038/nature20136, 2017.

Solgaard, A., Kusk, A., Merryman Boncori, J. P., Dall, J., Mankoff, K. D., Ahlstrøm, A. P., et al.: Greenland ice velocity maps from the PROMICE project, Earth Syst. Sci. Data, 13, 3491–3512, https://doi.org/10.5194/essd-13-3491-2021, 2021.

https://doi.org/10.5194/egusphere-2025-603
Preprint. Discussion started: 28 March 2025

Stanton, T. P., Shaw, W. J., Truffer, M., Corr, H. F. J., Peters, L. E., Riverman, K. L., et al.: Channelized ice melting in the ocean boundary layer beneath Pine Island Glacier, Antarctica, Science, 341, 1236–1239, https://doi.org/10.1126/science.1239373, 2013.

Still, H. and Hulbe, C.: Mechanics and dynamics of pinning points on the Shirase Coast, West Antarctica, The Cryosphere, 15, 2647–2665, https://doi.org/10.5194/tc-15-2647-2021, 2021.

Still, H., Campbell, A., and Hulbe, C.: Mechanical analysis of pinning points in the Ross Ice Shelf, Antarctica, Ann. Glaciol., 60, 32–41, https://doi.org/10.1017/aog.2018.31, 2019.

St-Laurent, P., Klinck, J. M., and Dinniman, M. S.: Impact of local winter cooling on the melt of pine island glacier, Antarctica, J. Geophys. Res. Oceans, 120, 6718–6732, https://doi.org/10.1002/2015JC010709, 2015.

Strozzi, T., Luckman, A., Murray, T., Wegmüller, U., and Werner, C.: Glacier motion estimation using sar offset-tracking procedures, IEEE Trans. Geosci. Remote Sens., 40, 2384–2391, https://doi.org/10.1109/TGRS.2002.805079, 2002.

Thoma, M., Jenkins, A., Holland, D., and Jacobs, S.: Modelling Circum Polar Deep water intrusions on the Amundsen Sea continental shelf, Antarctica, Geophys. Res. Lett., 35, L18602, https://doi.org/10.1029/2008GL034939, 2008.

Webber, B. G. M., Heywood, K. J., Stevens, D. P., Dutrieux, P., Abrahamsen, E. P., Jenkins, A., et al.: Mechanisms driving variability in the ocean forcing of pine island glaciers, Nat. Commun., 8, 14507, https://doi.org/10.1038/ncomms14507, 2017.

Wegmüller, U., Werner, C., Strozzi, T., Wiesmann, A., Frey, O., and Santoro, M.: Sentinel-1 support in the gamma software, Procedia Comput. Sci., 100, 1305–1312, https://doi.org/10.1016/j.procs.2016.09.246, 2016.

Werner, C. L., Wegmüller, U., Strozzi, T., and Wiesmann, A.: Gamma SAR and interferometric processing software, in Proceedings of the ERS645 ENVISAT Symposium, Gothenburg, Sweden, 16–20 October 2000, 1620, 1620, 2000.

Yoon, S. T., Lee, W. S., Nam, S., Lee, C. K., Yun, S., Heywood, K., et al.: Ice front retreat reconfigures meltwater-driven gyres modulating ocean heat delivery to an Antarctic ice shelf, Nat. Commun., 13, 306, https://doi.org/10.1038/s41467-022-27968-8, 2022.

Zhang, B., Liu, J., Wang, Z., Liu, T., and Yang, Q.: Antarctic ice-shelf thickness changes from CryoSat-2 SARIn mode measurements: Assessment and comparison with IceBridge and ICESat, J. Earth Syst. Sci., 129, 127, https://doi.org/10.1007/s12040-020-01392-2, 2020.

Zinck, A.-S. P., Wouters, B., Lambert, E., and Lhermitte, S.: Unveiling spatial variability within the Dotson Melt Channel through high-resolution basal melt rates from the Reference Elevation Model of Antarctica, The Cryosphere, 17, 3785–3801, https://doi.org/10.5194/tc-17-3785-2023, 2023a.

Zinck, A.-S. P.: BURGEE, [Software], GitHub, https://github.com/aszinck/BURGEE, 2023b.